Nuclear Engineering and Technology 54 (2022) 3855–3863

Contents lists available at ScienceDirect

Nuclear Engineering and Technology

journal homepage: www.elsevier.com/locate/net

Original Article

Particle loading as a design parameter for composite radiation shielding

N. Baumann [a], K. Marquez Diaz [a], K. Simmons-Potter [a], B.G. Potter Jr. [a, *], J. Bucay [b]

[a] University of Arizona, Tucson, AZ, 85721, USA
[b] Raytheon Technologies, San Diego, CA, USA

ARTICLE INFO

Article history:
Received 14 February 2022
Received in revised form
21 April 2022
Accepted 29 May 2022
Available online 1 June 2022

Keywords:
Radiation shielding
Monte carlo simulation
Additive manufacturing
Polymer composite

ABSTRACT

An evaluation of the radiation shielding performance of high-Z-particle-loaded polylactic acid (PLA) composite materials was pursued. Specimens were produced via fused deposition modeling (FDM) using copper-PLA, steel-PLA, and $BaSO_4$-PLA composite filaments containing 82.7, 75.2, and 44.6 wt% particulate phase contents, respectively, and were tested under broad-band flash x-ray conditions at the Sandia National Laboratories HERMES III facility. The experimental results for the mass attenuation coefficients of the composites were found to be in good agreement with GEANT4 simulations carried out using the same exposure conditions and an atomistic mixture as a model for the composite materials. Further simulation studies, focusing on the Cu-PLA composite system, were used to explore a shield design parameter space (in this case, defined by Cu-particle loading and shield areal density) to assess performance under both high-energy photon and electron fluxes over an incident energy range of 0.5 −15 MeV. Based on these results, a method is proposed that can assist in the visualization and isolation of shield parameter coordinate sets that optimize performance under targeted radiation characteristics (type, energy). For electron flux shielding, an empirical relationship was found between areal density (AD), electron energy (E), composition and performance. In cases where $\frac{E}{AD} \geq 2$ MeV•cm•g^{-1}, a shield composed of >85 wt% Cu results in optimal performance. In contrast, a shield composed of <10 wt% Cu is anticipated to perform best against electron irradiation when $\frac{E}{AD} < 2$ MeV•cm•g^{-1}.

1. Introduction

The development of radiation shields with tailored geometries, reduced mass and volume, and optimized radiation response, is a continuing challenge for microelectronic and optical subsystems operating on space-based platforms under varied radiation environments. Established shielding strategies based on bulk single-phase materials (metals, alloys, polymers) or layered assemblies of single-phase materials have been widely investigated [1–4]. Novel approaches using particle-loaded polymer composites, in which the particulate phase is a high-Z material dispersed within the low-Z polymer matrix, are also of great interest [5–18]. A multi-phase, multi-Z-number shield structure can offer efficient absorption of secondary radiation in one phase arising from the initial radiation interactions within another [1,2,18–22]. Moreover, the use of thermoplastic polymer matrices as the basis for a particle-loaded composite enables the application of fused deposition modeling (FDM)-based additive manufacturing to rapidly realize tailored shield geometries [11,20,22].

The efficacy of multiphase material shield designs is dependent upon a number of factors, including the specific radiation environment, the spatial distribution of phases within the composite, the relative phase content (e.g. weight ratio of high-Z to low-Z phase), and the overall areal density for the structure. A readily accessible framework within which to assess the performance of different shield designs is needed that would connect application-specific radiation environment and constraints imposed by application geometries and material processing compatibility.

In this context, the present work presents an evaluation of the effect of high-Z phase content in inorganic particle-polymer composites on shield performance. Here, the high-Z particle phase is uniformly distributed within the low-Z polymer matrix, providing direct correspondence to feedstocks often employed for FDM 3D printing. An initial experimental study using high dose-rate flash x-

* Corresponding author.
E-mail address: bgpotter@email.arizona.edu (B.G. Potter).

https://doi.org/10.1016/j.net.2022.05.029

ray fluxes at the Sandia National Laboratories HERMES III facility was used to establish the viability of the atomistic mixture material model used in GEANT4 as a means to predict the performance of the discrete, multiphase composite typical of the materials of interest here. GEANT4 modeling was then extended to explore a more generalized design space focusing on shielding performance under both gamma and electron fluxes with variation in particle-loading, shield areal density, and incident radiation energy [23].

Based on the modeling results, a visualization tool is proposed (in this case, a high-Z-phase content map) that enables the ready identification of shield design parameter combinations (high-Z phase content, radiation characteristics and shield areal density) that provide optimized performance. The approach developed here offers a basis from which to identify shield design candidates with common performance capabilities, enabling further assessment in terms of other constraints (e.g. geometry, mass) unique to the application environment.

2. Materials and methods

High-Z particle-polymer matrix composite shield behavior was examined via two primary efforts: a. an experimental verification of GEANT4 simulation results for 3D-printed, particle-loaded polymer composite structures, and b. the subsequent use of GEANT4 to explore shield performance within a design space defined by particle content in the composite, shield areal density, and radiation energy. The inorganic particle-polymer composite material FDM feedstocks examined experimentally were used as the basis for these latter computations.

2.1. Materials selection

Several commercially available high-Z particle-loaded polylactic acid (PLA) polymer FDM feedstocks were identified. Copper-loaded PLA, steel-loaded PLA (*ColorFabb*, Inc.) and $BaSO_4$-loaded PLA (*Nanovia*, Inc.) filaments were obtained and examined with scanning electron microscopy equipped with energy dispersive spectrometry (SEM/EDS) to confirm particle loading fraction, morphology, and distribution. See Table 1 for a summary of the characteristics found for the selected filaments.

Weight and volume percentages were calculated from the densities given in the manufacturers' datasheets using Equations (1)–(3). These three composites provided the basis for the initial experimental validation of GEANT4 performance.

$$\rho_c = \rho_A f_{V,A} + \rho_B\left(1 - f_{V,A}\right) \tag{1}$$

$$f_{W,A} = \frac{\rho_A}{\rho_c} f_{V,A} \tag{2}$$

$$\rho_c = \left(\frac{f_{W,A}}{\rho_A} + \frac{1 - f_{WA}}{\rho_B}\right)^{-1} \tag{3}$$

where ρ_A, ρ_B, and ρ_c are the densities of the high-Z particulate filler, low-Z matrix, and composite respectively. $f_{V,A}$ and $f_{W,A}$ are the volume and weight fractions of the high-Z particulate filler.

2.2. Fused deposition modeling

Samples for radiation testing were printed using an FDM 3D printer (Inventor, *FlashForge*). All samples were printed with a print speed of 60 mm/s, layer height of 0.18 mm, 3 shell layers, 100% infill, nozzle temperature of 210 °C, and bed temperature of 60 °C. A stepped geometry (see Fig. 1) was used to evaluate the radiation shielding performance at two different thicknesses (areal densities) to enable an experimental evaluation of effective mass attenuation coefficient over two shield thicknesses for each feedstock used. Each sample had a base of 25 mm × 50 mm, with the thicker step being 20 mm and the thinner step being 5–10 mm, depending on the material. These thickness values were anticipated to correspond to about a 10% and 20% reduction in total ionizing dose (TID) for the thin and thick steps respectively. Lighter regions in the SEM backscatter electron images of Fig. 1 correspond to the high-Z particles embedded in the PLA matrix. These images were analyzed to assess particle size distribution and loading levels for each of the commercial filaments. See Table 2 for a summary of specimen dimensions and particle loading information.

2.3. Radiation testing

Experimental performance of the printed shield materials was measured at the Sandia National Laboratories HERMES III (High-Energy Radiation Megavolt Electron Source) facility. HERMES III is a flash x-ray source with an average photon energy of 1.9 MeV (tantalum converter), 21 ns FWHM pulse, and an exposure area of approximately 4.5 m^2. Total ionizing dose (TID) is the summation of the overall accumulated dose from various sources (electrons, protons, heavy ions, x-rays, gamma rays, etc.), measured in Rads (0.01 J/kg). The TID was measured using CaF thermoluminescent dosimeters (TLDs) placed directly behind the thin and thick steps (TID_{sample}) and on the incident face ($TID_{reference}$) of the sample. TLDs were calibrated for the HERMES III spectral output which also served as the incident radiation characteristics for subsequent GEANT4 modeling. The effective mass attenuation coefficient was calculated using the Beer-Lambert law shown in Equation (4).

$$\left(\frac{\mu}{\rho}\right)_{eff} = -\frac{1}{x\rho}\ln\left(\frac{I}{I_0}\right) \cong -\frac{1}{AD}\ln\left(\frac{TID_{sample}}{TID_{reference}}\right) \tag{4}$$

where μ is the linear attenuation coefficient in cm^{-1}, x is the step thickness in cm, ρ is the mass density in g/cm^3, $\frac{I}{I_0}$ is the transmissivity, AD is the areal density in g/cm^2, and $\frac{TID_{sample}}{TID_{reference}}$ is the fractional TID.

Experimentally determined mass attenuation coefficients for each of the 3D printed particle-composite materials were compared with GEANT4-based simulations.

2.4. Computational simulations

All simulations in the present study were run using GEANT4

Table 1
Loading characteristics of the selected commercial high-Z loaded filaments.

Composite System	Wt.% high-Z Filler	vol% high-Z Filler	High-Z Particle Size (μm)
Cu-PLA	82.7	37.0	20–50
Steel-PLA	75.2	29.5	20–50
$BaSO_4$-PLA	44.6	16.5	0.2–1

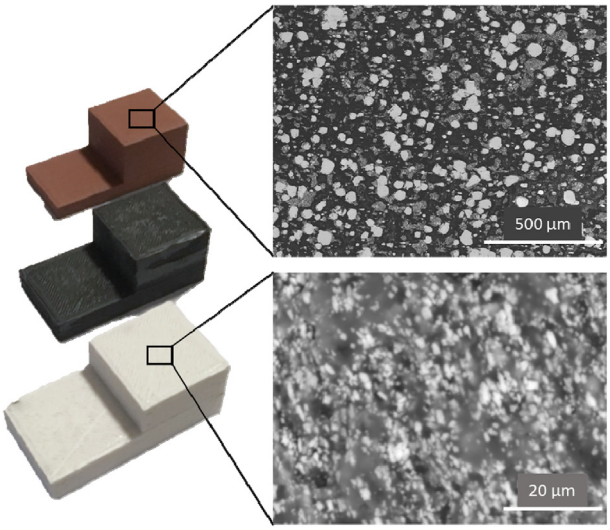

Fig. 1. Left: Photograph of the samples of commercial filaments printed for radiation testing at HERMES III. From top to bottom: copper-loaded, steel-loaded, and $BaSO_4$-loaded filaments. Insets show SEM micrographs (back-scatter electron configuration) of as-printed copper-loaded and $BaSO_4$-loaded filaments.

v10.7, an open-source Monte Carlo simulation software for high energy physics [23]. A listing of data libraries included in the GEANT4 distribution used can be found at https://geant4.web.cern.ch/support/data_files_citations [24]. GEARS (***G**eant4 **E**xample **A**pplication with **R**ich features yet **S**mall footprint*) was used to run GEANT4 entirely via plain text geometry descriptions and UI command macros [25]. The "Shielding" physics list was used for all simulations [26]. This list is based on the FTFP-BERT physics list with additional physics processes relevant to radiation shielding. A complete list of the GEANT4 physics libraries utilized in "Shielding" can be found in the source code for Shielding.cc at https://github.com/Geant4/geant4/blob/master/source/physics_lists/lists/src/Shielding.cc [27]. The object-oriented data processing framework, ROOT, was used to analyze the simulation results [28]. To quantify shield performance in the simulations, the detector was defined as the sensitive volume. From this, statistics including total counts, energy spectrum, and mean energy of absorbed radiation can be extracted. All simulations were run and data were processed using an 11th generation Intel® Core ™ i7-10750H CPU running at 2.6 GHz and equipped with 8 GB of RAM.

GEANT4 simulations addressed the computation of 3D-printed composite gamma shielding behavior under HERMES III experimental conditions for the three high-Z-particle-PLA composite formulations described above. A subsequent simulation study was used to explore a shield design space using the Cu-particle filled PLA composite material as a model system. Simulation conditions and details for each effort are provided below, including the number of incident particles used and uncertainty quantifications.

2.4.1. HERMES III simulations

The HERMES III source and geometry setup were simulated in GEANT4 to compare with the experimental results described above. To maintain consistency with the HERMES III broad band spectral source and the experimental geometry described in Sections 2.2 and 2.3 each sample was irradiated with a 10 cm diameter, circular, collimated, planar beam with the same energy spectrum as the HERMES III source (see Fig. 2). Because the beam diameter is large (10 cm) compared to the samples (5 cm), 10^8 particles were simulated for each material to achieve counts above 10^4 at the detector. Instead of the traditional narrow beam geometry used for measuring gamma attenuation, the total absorbed energy for each TLD was extracted instead to mimic the experiment as closely as possible. Models of the experimental stepped samples and CaF TLDs were constructed using the GEANT4 geometry text file description [29]. The commercial filament materials were defined as custom material descriptions with relative compositions consistent with SEM/EDS confirmed compositions. The TLDs were placed behind the sample identically to the experimental setup, and the reference TLD was placed adjacent to the sample as shown in Fig. 2. The total absorbed energy in the TLDs, or total ionizing dose (TID) was calculated for comparison with the experimental results. The simulation uncertainty was calculated by running 20 identical simulations while changing the random number generator (RNG) seed value for each run. The error bars for the HERMES simulations indicate the 95% confidence interval (2 standard deviations). As expected for Monte Carlo simulations, the uncertainty is proportional to the square root of the measured TID.

2.4.2. Design study simulations

Subsequent simulation efforts focused on the exploration of a limited shield design parameter space. Particle loading and shield areal density were examined in the context of the copper-particle loaded PLA system under gamma and electron incident flux. Homogenous mixtures with varied copper loading levels were simulated in GEANT4 in steps of 5 wt% Cu from 0% (pure PLA) to 100% (pure Cu). Samples consisted of 20 cm diameter disks, with areal densities of 1, 2, 5, 6, 8, and 10 g/cm^2. A hemispherical sodium iodide detector with a wall thickness of 1 cm was placed directly behind the sample, as shown in Fig. 3. Each sample was irradiated with a 2 cm diameter circular, planar, collimated beam of 0.1, 0.5, 1, 2, 5, 10, 12, and 15 MeV gamma photons and electrons. In this case, simulations were pursued using 10^5 incident particles in the simulation. The uncertainty in the resulting TID values was calculated from the standard deviation of 20 identical simulations run with different starting RNG seed values. For 10^5 electrons, the uncertainty in the TID returned was ±0.059% of the average. As a check, simulations using 10^6 incident particles were run and found to produce a ±0.016% uncertainty. The reduction in uncertainty by a factor of 3.7 was accompanied, however, by an increase in computation time by a factor of 13.6 using the resources available for the study. In this context, simulations using 10^5 incident particles were considered sufficient to establish trends in performance with shield design variation and to provide initial insight into relevant TID levels.

Table 2
Physical properties of the commercial off-the-shelf (COTS) filaments and the HERMES III sample dimensions.

Composite System	Mass (g)	Thin step (cm)	Thick Step (cm)	Volume (cm^3)	Density (g/cm^3), experimental (built object)	Density (g/cm^3), filament (source: vendor data sheet)
Cu-PLA	59.595 ± 0.005	0.52 ± 0.01	2.02 ± 0.01	15.4 ± 0.5	3.87 ± 0.13	4.00
Steel-PLA	57.716 ± 0.005	0.77 ± 0.01	2.07 ± 0.01	17.7 ± 0.5	3.26 ± 0.09	3.13
$BaSO_4$-PLA	32.877 ± 0.005	1.06 ± 0.01	2.07 ± 0.01	19.7 ± 0.5	1.67 ± 0.04	1.66

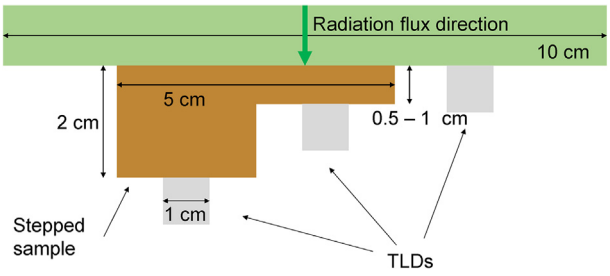

Fig. 2. Schematic of simulation geometry used for the validation of simulation results of commercial feedstocks. A large beam covering the entire simulation geometry was used to mimic the conditions of the HERMES III source relative to the specimen under test. Flux direction is top-to-bottom. Three CaF thermoluminescent detectors (TLDs) were used to collect the total ionizing dose.

Total ionizing dose (TID) was used as a primary shield performance metric for all simulations. TID was calculated by multiplying the number of absorbed particles in the detector by their mean energy. In addition to primary radiation flux traversing the shield thickness, TID will also include contributions from secondary electrons and gamma photons that can be generated upon interaction with the shield material. The absolute TID values computed are dependent upon incident flux (scaling with the number of particles used to define the incident beam), the specifics of the specimen and collection geometry and the detector material and thickness employed. However, trends in TID magnitude are of primary interest in this case to provide a relative assessment of shield performance. In this context, a lower TID is considered more favorable.

3. Results

3.1. Radiation testing

A comparison between the experimentally obtained HERMES III test data results and the corresponding GEANT4 simulation described above is provided in Fig. 4 for the commercially available FDM feedstock materials. The average experimental effective mass attenuation coefficients are 0.028, 0.039, and 0.046 cm^2/g for the copper-loaded, steel-loaded, and $BaSO_4$-loaded filaments respectively. The average simulation effective mass attenuation coefficients were 0.043, 0.039, and 0.062 cm^2/g respectively. Greater uncertainties in the experimentally determined attenuation coefficients are observed in Fig. 4 for the thinner thickness (lower areal density) measurement locations. These higher uncertainties are associated with the inherent measurement uncertainty of the TLDs (estimated at 10%). These uncertainties dominate at the lower attenuation levels associated with the thinner portion of the experimental specimens. Within the thicker (higher areal density) portion of the specimens (in which the experimental uncertainty associated with the mass attenuation coefficient is reduced), the errors between the simulated and experimental mass attenuation coefficients were found to be 28.8% for the copper-loaded-PLA, 3.0% for the steel-loaded-PLA, and 10.8% for the $BaSO_4$-loaded PLA feedstocks. While not a focus in the present study, no physical degradation in the specimens was observed after gamma exposure in the specimens. We expect to examine this issue of shield resilience in future studies.

3.2. Design study simulations

3.2.1. Gamma irradiation

Fig. 5a provides an overview of the shield parameter space and resulting TID simulated for a Cu-particle-filled PLA composite feedstock. The effects of particle loading and shield areal density are shown. Overall, the TID is found to increase by over an order of magnitude with increasing energy. Fig. 5b and c contain examples of constant Cu-loading (at 50 wt%) and constant areal density (at 5 g/cm^2) slices, respectively, through the TID plot in Fig. 5a. Referring to Fig. 5b, within the energy range 0.5–5 MeV, the TID drops monotonically with increasing areal density, decreasing from 1.27×10^{-4} to 1.04×10^{-4} Rad for areal densities of 1 and 10 g/cm2, respectively, in a 40 wt% Cu loading level under 2 MeV incident energy. At higher energies (>5 MeV) a reduction in TID is observed at the lower areal densities (decreasing from 8.82×10^{-4} to 7.75×10^{-4} Rad over the areal density range of 2 to 1 g/cm^2, respectively, in a 50 wt% Cu loading level under 15 MeV electrons). This latter observation is likely an indicator of the contribution of secondary particle generation effects from within the shield to the high TID magnitudes at these energies.

Referring to Fig. 5c, the particle loading level appears to have only a limited impact on TID for gamma energies below 5 MeV. Increased sensitivity to Cu loading is observed for the highest gamma energies examined with a lower Cu content resulting in a reduction in TID, with an average of 13% lower TID across all areal densities for pure PLA compared to pure Cu at 15 MeV. As gamma energy decreases, the difference in TID between the compositional extremes decreases to less than 2% on average for 2 MeV, and less than 1% for 0.5 MeV.

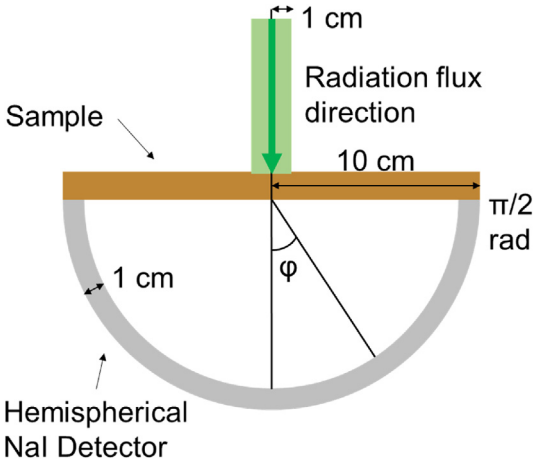

Fig. 3. Schematic of simulation geometry used for the compositional study. Flux direction is top-to-bottom. The sensitive area of the entire hemisphere was used to measure the total ionizing dose for both electrons and gamma. The total energy absorbed into the detector was measured across ϕ from 0 to $\pi/2$ radians.

3.2.2. Electron irradiation

Fig. 6 provides a corresponding summary of shield performance with shield parameters, now under electron irradiation. In this case, areal density and Cu loading (wt.%), are again explored. As expected, lower areal density shield designs tend to perform poorer (higher TID values). Conversely, a general enhancement of shield performance (lower TID) can be observed with a reduction in Cu loading level across all but the lower electron energies examined (e.g. 0.5 and 1 MeV). In Fig. 6, a significant transition in TID behavior with areal density can be observed under higher energy electron flux (5, 10, 12, 15 MeV) with increasing areal density resulting in a significant reduction in TID. Fig. 7 shows constant-areal-density slices through the three-dimensional graphic in Fig. 6. Black circles on the TID vs. Cu content graphs show the progression of the minimum TID value (i.e. optimized shield composition at that areal

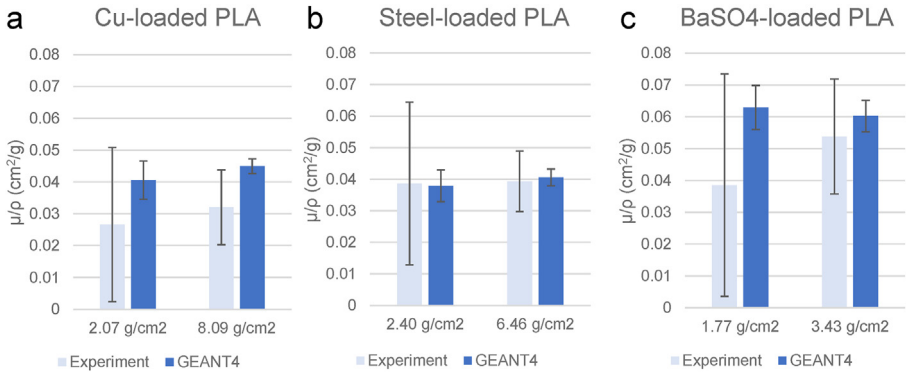

Fig. 4. a–c: Comparison of HERMES III experimental results with GEANT4 simulations. The computed effective mass attenuation coefficients for the copper-loaded, steel-loaded, and $BaSO_4$-loaded filaments are shown in (a–c) respectively.

density and energy) toward the lower Cu content (PLA rich). For higher incident electron energies and lower areal densities (below 5 g/cm^2, see Fig. 7a and b) the pure copper phase shield (100 wt% Cu) performs best (i.e., exhibits a minimum TID). As areal density increases (Fig. 7c–f), the composition corresponding to a minimum TID shifts from copper rich to PLA rich. This transition is especially evident moving from 5 to 6–8 g/cm^2 (Fig. 7c–e). Thus, as the composite shield's areal density increases, the impact of high-Z Cu particle loading on shield performance decreases.

4. Discussion

4.1. Radiation testing and simulation verification

As shown in Fig. 4, the HERMES III simulations show good agreement with the experimental results, despite the large uncertainties associated with the TLD detectors used in the experiment. The uncertainty associated with the HERMES III simulation results are discussed in Section 2.4.1. Because the TLDs were not shielded from the sides or back, scattered or secondary radiation generated from ancillary mounting equipment and surrounding environment could have contributed to local TLD response. Additionally, because the Cu-loaded sample was only 96.7% dense, the remaining porosity (air gaps) due to 3D printing flaws (e.g. cracking, delamination) could also reduce the performance in the experiment. That said, the cross-sectional SEM examination of the specimens (Fig. 1) did not reveal significant contributions from larger length scale microstructural discontinuities. The large uncertainty in the thin step experimental values is due to a minimal reduction in TID combined with the large uncertainty of the experimental TLDs (estimated at between 4 and 10%). As the reduction in TID increases for the thicker portion of the specimen, the uncertainty was noticeably reduced.

It is important to note that, while the FDM-produced materials are discrete particle-matrix composites with finite high-Z particle sizes, the plain text geometry description in GEANT4 creates homogenous atomistic mixtures. Simulation of a dispersed phase composite in GEANT4 would be prohibitively time intensive since at the particle sizes listed in Table 1, there are ~10^7 particles/cm^3 for the copper and steel-loaded filaments, and ~10^{12} particles/cm^3 for the $BaSO_4$ filament. The good agreement between GEANT4 and experimental data suggest the viability of approximating spatially distinct, homogeneously distributed second-phase particles with atomistic mixtures in the simulation as well as the limited impact of microstructural imperfections (build-defects) on the performance of the specimens examined The impact of a heterogeneous spatial distribution of high-Z second phase on radiation performance, e.g. stratification normal to the flux, is the focus of ongoing work.

4.2. Design study simulations

Figs. 5 and 6 provide an effective means to visualize the interrelationship between radiation environment characteristics (type, energy) and shield design parameters (areal density, Cu-loading) leading to shield performance. As described in the Results, the

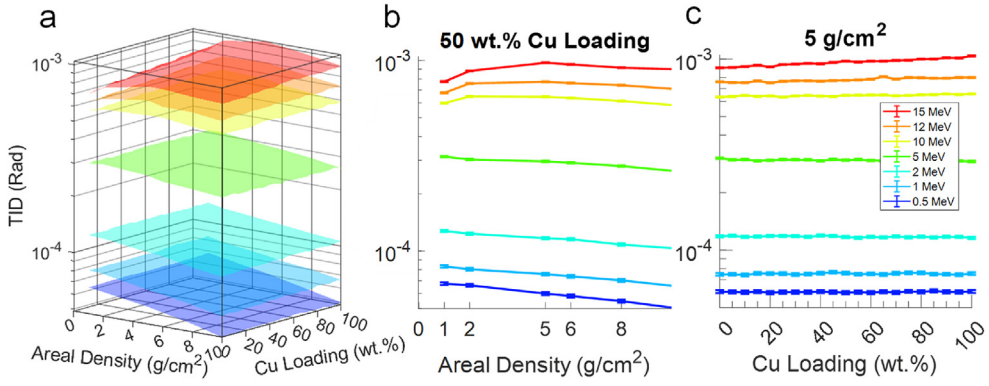

Fig. 5. a–c: Cu-PLA simulated TID under gamma irradiation at 0.5, 1, 2, 5, 10, 12, and 15 MeV from bottom to top as functions of areal density and copper loading. Fig. 5a shows the TID contours, while 5b and 5c show constant-compositional (50 wt%) and constant areal density (5 g/cm^2) cuts of 5a, respectively.

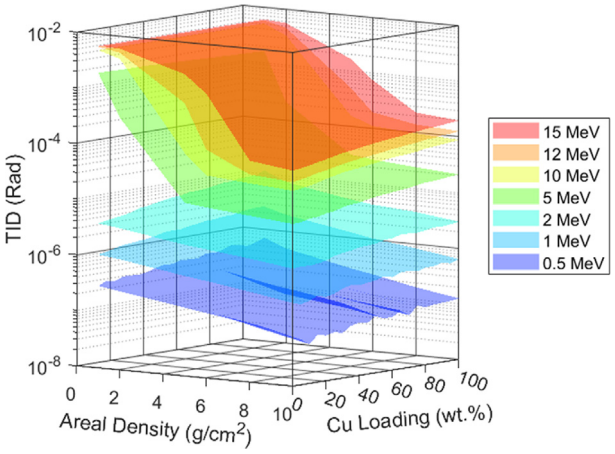

Fig. 6. Cu-PLA simulated TID under electron irradiation at 0.5, 1, 2, 5, 10, 12, and 15 MeV from bottom to top as functions of areal density and copper loading.

sensitivity of TID to changes in copper loading under gamma radiation were limited over a majority of the gamma energies included in the simulation. This behavior is consistent with the long effective mean free path for gamma photons within these materials relative to the comparatively smaller shield thicknesses examined in the present study. This disparity limited the probability for significant interactions between the incident flux and material (regardless of Cu-loading) within the shield volume. This can be an important factor, for example, in the assessment of potential shield designs where mass reduction may be of primary interest. TID was also found to have a weak dependence on areal density.

In contrast, for the case of electron flux (Fig. 6), the TID exhibits a dependence on areal density that becomes more nonlinear in nature at greater electron energies. This is a critical finding for electron radiation shielding design and is in contrast to prediction based on database information, e.g. NIST ESTAR (***E**lectron **St**opping powers **A**nd **R**anges)* [30] which assumes that performance is constant when normalized for areal density. Accurate prediction of shield design criteria is of key interest in radiation shielding for microelectronics as performance is measured in units derived from total ionizing dose, a primary cause of failure in space-based microelectronics [31,32].

In addition to the identification of general trends of shield behavior with variation in composition, areal density and energy, the simulation results (Figs. 5 and 6), obtained can be used to provide more specific design guidance for the performance optimization of shields constructed using the high-Z-particle-polymer based composite. Focusing on material composition (in this case, related to particle loading in the composite), Fig. 8 provides a means to visualize the shield design space based on incident radiation characteristics (type and energy) and mass/volume constraints (through the areal density). In this case, Fig. 8 depicts a "minimum-TID" compositional map (Cu-loading values) within the areal density/radiation energy coordinate space. Shading in the map indicates those Cu loading levels that provide minimized TID values for the corresponding shield designs. For example, in the case of Fig. 8b (electron flux results), the plot is obtained by fitting a 2D surface to the minima coordinates (black dots) shown in Fig. 7 for each energy and areal density combination. Clearly, a complementary set of areal density maps could be produced from the simulation data in Cu-loading/energy coordinate space to provide a direct means to assess potential areal density values (corresponding most directly to shield thickness) that would minimize TID.

Visualizations such as those of Fig. 8, created by reduction of the GEANT4 simulation results, offer a rapid means to identify candidate shield designs. For example, for a given incident radiation energy, a set of areal density-Cu loading combinations can be directly visualized that will correspond to minima in TID. Application-specific constraints on shield design, e.g. specific feedstock availability or printability; mass or volume limitations, can then be used to restrict the range of Cu-loading levels and areal densities to those suitable for the application. Once a collection of

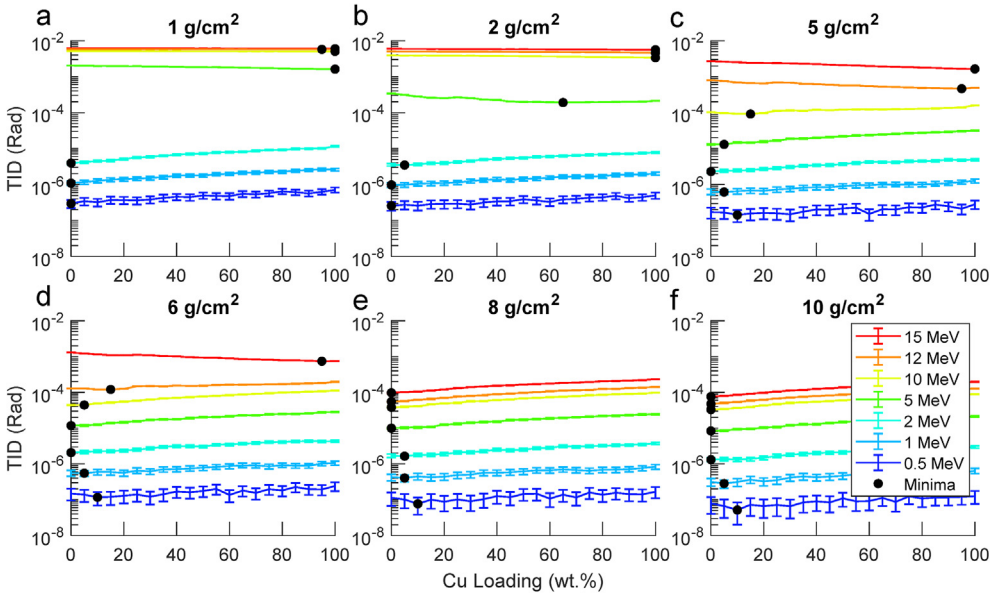

Fig. 7. a–f: Constant areal density plots from Fig. 6 of TID as function of composition over the range of incident electron energies examined. Graphs a-f correspond to areal densities of 1, 2, 5, 6, 8, and 10 g/cm^2 respectively. The minimum TID values for each energy are marked with black circles. Energies from top to bottom in each plot are 15, 12, 10, 5, 2, 1, and 0.5 MeV, as shown in the legend of graph (a).

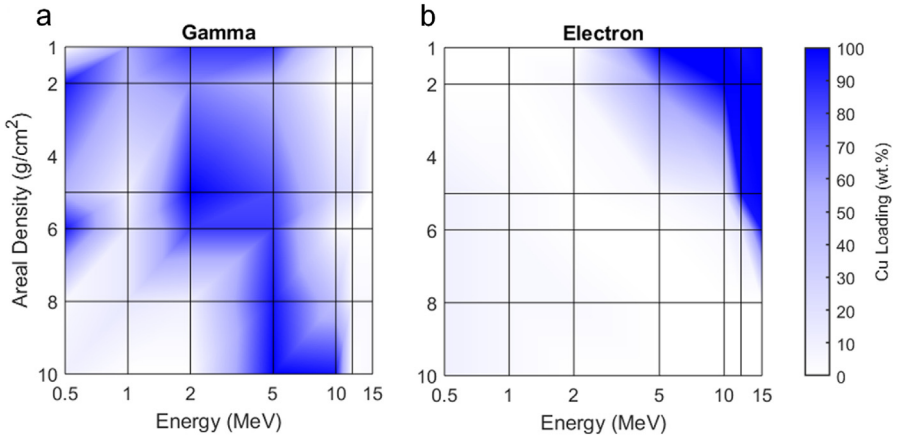

Fig. 8. (a) Compositional map (Cu-loading) corresponding to local TID minima under gamma irradiation as a function of areal density and energy. (b) Compositional map (Cu-loading) corresponding to local TID minima under electron irradiation as functions of areal density and energy. Each composition in the field represents the point of maximum shield performance at each energy-areal density pair.

shield parameter sets is identified using the maps in Fig. 8, the corresponding shield performance (TID) values can be readily obtained from the original simulation data set (Fig. 5 or 6) to quantify performance and rank different shield design options. This general approach can be readily extended to other feedstocks and radiation types.

Using such an approach, it can be seen that for electron irradiation, a pure copper radiation shield will outperform a pure PLA shield by over 25% at an areal density of 1 g/cm^2 (equal mass) for energies >10 MeV. Empirically, it was observed that high-Z dominant shielding will have the highest performance against electron irradiation for electron energy (E) and areal density (AD) when $\frac{E}{AD} \geq$ 2 MeV•cm•g^{-1}. This empirical relationship, visualized in Fig. 9, provides a streamlined yet powerful design parameter for electron radiation shielding.

From an application perspective, the flux of electrons >10 MeV in LEO is two to four orders of magnitude lower than the flux of ≤2 MeV electrons [33,34]. Thus, the majority of electrons that contribute to the total ionizing dose are shielded with compositions in the printability range of commercial FDM 3D printers. In general,

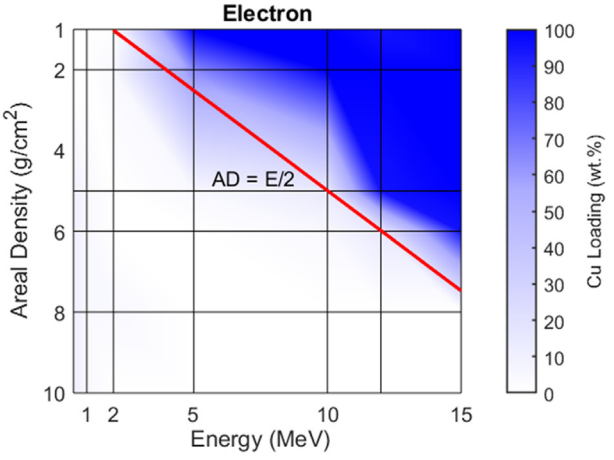

Fig. 9. The data of Fig. 8b, with electron energy plotted on a linear scale. The red line represents the function AD = 1/2E. When E/AD≥2 MeV cm g^{-1}, high-Z dominant (high Cu loading) compositions outperform low-Z dominant ones. (For interpretation of the references to colour in this figure legend, the reader is referred to the Web version of this article.)

a loading of ≤10 wt% copper in PLA performs the best over the energy ranges comparable to typical space radiation environments. The copper-loaded filament examined in this study is 82.7 wt% Cu, so a filament in the 10 wt% range would be easily printable. A loading in that range can be achieved by creating a custom filament via dual screw extrusion or via a layered PLA and copper-loaded filament structure [35].

5. Conclusion

The present work demonstrates the simulation of additively manufacturable radiation shielding materials. Using GEANT4, good agreement was obtained with experimentally determined gamma mass attenuation coefficients obtained from FDM printed particle-PLA composite specimens with varied particle compositions, verifying the applicability of GEANT4 for the simulation of radiation effects in such discrete particle-matrix composite systems.

Radiation shielding performance over a multivariable space connecting operational conditions and shield characteristics (e.g., composition, areal density, radiation energy) was also examined. In the present case, effective radiation shielding candidates using copper-loaded PLA were found to correspond to filament compositions within the printable range of commercially available FDM 3D printers. For gamma or X-ray shielding below 10 g/cm^2 and at energies above 0.5 MeV (as studied here), there is minimal performance improvement achieved with Cu-PLA composite material compositions examined, as illustrated in Fig. 5c. In this case, the range of areal densities examined (1–10 g/cm^2) are shorter than the photon mean free path for the energies studied (0.5–15 MeV). The photon mean free paths were estimated from the NIST XCOM database (by taking the inverse of the gamma mass attenuation coefficient), ranging from 11 to 55 g/cm^2 over the investigated energy range [36]. Therefore, the probability for photon-matter interactions within the shield designs examined is low. In contrast, the electron mean free paths over the same energy range (estimated from the continuous slowing down approximation (CSDA) range from the NIST ESTAR database) are 0.2–8 g/cm^2 [30]. No clear trends in TID with respect to either energy or areal density are observed under gamma radiation due to this discrepancy between shield thickness and gamma mean free path.

Further, a method to visualize optimal shield material compositions (i.e. particle loading level) involved the development of compositional maps within energy-areal density space that depicted particle loading levels corresponding to a TID minimum

downstream of the shield. From this construction for electron irradiation, an empirical relationship connecting radiation energy and areal density was found to define a boundary separating high and low Cu-loading regions leading to improved shield performance. In this case, if the ratio of E/AD is greater than 2 MeV•cm g^{-1}, a composite with a high-Z phase content (>85 wt% Cu) would be most effective. Conversely, if E/AD < 2 MeV•cm g^{-1}, optimal shield performance can be attained with a majority low-Z composite (<10 wt% Cu). The use of a mapping strategy, as illustrated in Fig. 8, for any composite of low-Z and high-Z materials can help to establish key design criteria to reduce shield development time and minimize costly radiation testing.

Declaration of competing interest

The authors declare that they have no known competing financial interests or personal relationships that could have appeared to influence the work reported in this paper.

Acknowledgements

The authors thank Raytheon Technologies for their financial support of this work and Dr. Steve Manson at Raytheon Technologies for helpful discussions. The authors also wish to thank Sandia National Labs, HERMES III personnel and Dr. Stephen Tobin at Los Alamos National Laboratories for enabling the ride-along portion of the experimental testing.

References

[1] W.C. Fan, C.R. Drumm, G.J. Scrivner, Shielding considerations for satellite microelectronics, IEEE Trans. Nucl. Sci. 43 (1996) 2790–2796. https://ieeexplore.ieee.org/ielx1/23/12152/00556868.pdf?tp=&arnumber=556868&isnumber=12152.

[2] Z.D. Whetstone, K.J. Kearfott, Layered shielding design for an active neutron interrogation system, Radiat. Phys. Chem. 125 (2016) 69–74, https://doi.org/10.1016/j.radphyschem.2016.03.018.

[3] M. Arif Sazali, N.K. Alang Md Rashid, K. Hamzah, A review on multilayer radiation shielding, IOP Conf. Ser. Mater. Sci. Eng. 555 (2019), https://doi.org/10.1088/1757-899X/555/1/012008.

[4] G. Hu, H. Hu, Q. Yang, B. Yu, W. Sun, Study on the design and experimental verification of multilayer radiation shield against mixed neutrons and γ-rays, Nucl. Eng. Technol. 52 (2020) 178–184, https://doi.org/10.1016/j.net.2019.07.016.

[5] M.A. Ryder, D.A. Lados, G.S. Iannacchione, A.M. Peterson, Fabrication and properties of novel polymer-metal composites using fused deposition modeling, Compos. Sci. Technol. 158 (2018) 43–50, https://doi.org/10.1016/j.compscitech.2018.01.049.

[6] G. Almisned, F. Akman, W.S. Abushanab, H.O. Tekin, M.R. Kaçal, S.A.M. Issa, H. Polat, M. Oltulu, A. Ene, H.M.H. Zakaly, Novel Cu/Zn reinforced polymer composites: experimental characterization for radiation protection efficiency (rpe) and shielding properties for alpha, proton, neutron, and gamma radiations, Polymers 13 (2021), https://doi.org/10.3390/polym13183157.

[7] H.O. Tekin, M.R. Kaçal, S.A.M. Issa, H. Polat, G. Susoy, F. Akman, O. Kilicoglu, V.H. Gillette, Sodium dodecatungstophosphate hydrate-filled polymer composites for nuclear radiation shielding, Mater. Chem. Phys. 256 (2020), 123667, https://doi.org/10.1016/j.matchemphys.2020.123667.

[8] M.R. Kaçal, H. Polat, M. Oltulu, F. Akman, O. Agar, H.O. Tekin, Gamma shielding and compressive strength analyses of polyester composites reinforced with zinc: an experiment, theoretical, and simulation based study, Appl. Phys. Mater. Sci. Process 126 (2020) 1–15, https://doi.org/10.1007/s00339-020-3382-2.

[9] H.O. Tekin, F. Akman, S.A.M. Issa, M.R. Kaçal, O. Kilicoglu, H. Polat, Two-step investigation on fabrication and characterization of iron-reinforced novel composite materials for nuclear-radiation shielding applications, J. Phys. Chem. Solid. 146 (2020), 109604, https://doi.org/10.1016/j.jpcs.2020.109604.

[10] F. Akman, I. Ozkan, M.R. Kaçal, H. Polat, S.A.M. Issa, H.O. Tekin, O. Agar, Shielding features, to non-ionizing and ionizing photons, of FeCr-based composites, Appl. Radiat. Isot. 167 (2021), 109470, https://doi.org/10.1016/j.apradiso.2020.109470.

[11] Q. Li, Q. Wei, W. Zheng, Y. Zheng, N. Okosi, Z. Wang, M. Su, Enhanced radiation shielding with conformal light-weight nanoparticle-polymer composite, ACS Appl. Mater. Interfaces 10 (2018) 35510–35515, https://doi.org/10.1021/acsami.8b10600.

[12] S. Woosley, N. Abuali Galehdari, A. Kelkar, S. Aravamudhan, Fused deposition modeling 3D printing of boron nitride composites for neutron radiation shielding, J. Mater. Res. 33 (2018) 3657–3664, https://doi.org/10.1557/jmr.2018.316.

[13] Y. Wu, Y. Cao, Y. Wu, D. Li, Neutron shielding performance of 3D-Printed boron carbide PEEK composites, Materials 13 (2020), https://doi.org/10.3390/ma13102314.

[14] C.M. Shemelya, A. Rivera, A.T. Perez, C. Rocha, M. Liang, X. Yu, C. Kief, D. Alexander, J. Stegeman, H. Xin, R.B. Wicker, E. MacDonald, D.A. Roberson, Mechanical, electromagnetic, and X-ray shielding characterization of a 3D printable tungsten–polycarbonate polymer matrix composite for space-based applications, J. Electron. Mater. 44 (2015) 2598–2607, https://doi.org/10.1007/s11664-015-3687-7.

[15] A. Canel, H. Korkut, T. Korkut, Improving neutron and gamma flexible shielding by adding medium-heavy metal powder to epoxy based composite materials, Radiat. Phys. Chem. 158 (2019) 13–16, https://doi.org/10.1016/j.radphyschem.2019.01.005.

[16] A.M. El-Khatib, M.S. Hamada, M.T. Alabsy, Y.M. Youssef, M.A. Elzaher, M.S. Badawi, M. Fayez-Hassan, Y.N. Kopatch, I.N. Ruskov, M.I. Abbas, Fast and thermal neutrons attenuation through micro-sized and nano-sized CdO reinforced HDPE composites, Radiat. Phys. Chem. 180 (2021), 109245, https://doi.org/10.1016/j.radphyschem.2020.109245.

[17] M. Nabipour, B. Akhoundi, A. Bagheri Saed, Manufacturing of polymer/metal composites by fused deposition modeling process with polyethylene, J. Appl. Polym. Sci. 48717 (2019) 1–9, https://doi.org/10.1002/app.48717.

[18] X. Zhang, X. Zhang, S. Guo, Simple approach to developing high-efficiency neutron shielding composites, Polym. Eng. Sci. 59 (2019) E348–E355, https://doi.org/10.1002/pen.25065.

[19] X. Li, D. Warden, Y. Bayazitoglu, Analysis to evaluate multilayer shielding of galactic cosmic rays, J. Thermophys. Heat Tran. 32 (2018) 525–531, https://doi.org/10.2514/1.T5292.

[20] J. Wrobel, R. Hoyt, J. Cushing, M. Jaster, N. Voronka, J. Slostad, L. Paritsky, Versatile structural radiation shielding and thermal insulation through additive manufacturing, 27th Annu. AIAA/USU Conf. Small Satell. (2013) 1–9. http://digitalcommons.usu.edu/cgi/viewcontent.cgi?article=2926&context=smallsat.

[21] T. Gutu, Assessment of Polybenzimidazole Polymer Matrix Composite Constructed as a Graded-Z Laminate for Use as a Structural Radiation Shield for Cislunar Habitation Modules, University of Massachusetts Lowell, 2020.

[22] M. DeVanzo, R.B. Hayes, Ionizing radiation shielding properties of metal oxide impregnated conformal coatings, Radiat. Phys. Chem. 171 (2020), 108685, https://doi.org/10.1016/j.radphyschem.2020.108685.

[23] S. Agostinelli, J. Allison, K. Amako, J. Apostolakis, H. Araujo, P. Arce, M. Asai, D. Axen, S. Banerjee, G. Barrand, F. Behner, L. Bellagamba, J. Boudreau, L. Broglia, A. Brunengo, H. Burkhardt, S. Chauvie, J. Chuma, R. Chytracek, G. Cooperman, G. Cosmo, P. Degtyarenko, A. Dell'Acqua, G. Depaola, D. Dietrich, R. Enami, A. Feliciello, C. Ferguson, H. Fesefeldt, G. Folger, F. Foppiano, A. Forti, S. Garelli, S. Giani, R. Giannitrapani, D. Gibin, J.J. Gomez Cadenas, I. Gonzalez, G. Gracia Abril, G. Greeniaus, W. Greiner, V. Grichine, A. Grossheim, S. Guatelli, P. Gumplinger, R. Hamatsu, K. Hashimoto, H. Hasui, A. Heikkinen, A. Howard, V. Ivanchenko, A. Johnson, F.W. Jones, J. Kallenbach, N. Kanaya, M. Kawabata, Y. Kawabata, M. Kawaguti, S. Kelner, P. Kent, A. Kimura, T. Kodama, R. Kokoulin, M. Kossov, H. Kurashige, E. Lamanna, T. Lampen, V. Lara, V. Lefebure, F. Lei, M. Liendl, W. Lockman, F. Longo, S. Magni, M. Maire, E. Medernach, K. Minamimoto, P. Mora de Freitas, Y. Morita, K. Murakami, M. Nagamatu, R. Nartallo, P. Nieminen, T. Nishimura, K. Ohtsubo, M. Okamura, S. O'Neale, Y. Oohata, K. Paech, J. Perl, A. Pfeiffer, M.G. Pia, F. Ranjard, A. Rybin, S. Sadilov, E. di Salvo, G. Santin, T. Sasaki, N. Savvas, Y. Sawada, S. Scherer, S. Sei, V. Sirotenko, D. Smith, N. Starkov, H. Stoecker, J. Sulkimo, M. Takahata, S. Tanaka, E. Tcherniaev, E. Safai Tehrani, M. Tropeano, P. Truscott, H. Uno, L. Urban, P. Urban, M. Verderi, A. Walkden, W. Wander, H. Weber, J.P. Wellisch, T. Wenaus, D.C. Williams, D. Wright, T. Yamada, H. Yoshida, D. Zschiesche, GEANT4 - a simulation toolkit, Nucl. Instruments Methods Phys. Res. Sect. A Accel. Spectrometers, Detect. Assoc. Equip. 506 (2003) 250–303, https://doi.org/10.1016/S0168-9002(03)01368-8.

[24] CERN, Credit/citations for data files distributed with Geant4 (n.d.), https://geant4.web.cern.ch/support/data_files_citations. (Accessed 15 April 2022).

[25] J. Liu, GEARS [source code], https://github.com/jintonic/gears, 2021.

[26] D. Wright, Shielding physics list description. https://www.slac.stanford.edu/comp/physics/geant4/slac_physics_lists/shielding/physlistdoc.html, 2012. (Accessed 20 December 2021).

[27] T. Koi, G. Folger, Shielding.cc [source code], https://github.com/Geant4/geant4/blob/master/source/physics_lists/lists/src/Shielding.cc, 2010. (Accessed 10 April 2022).

[28] R. Brun, F. Rademakers, Root - an object oriented data analysis framework, in: Proc. AIHENP'96 Work., 1996, pp. 81–86, https://doi.org/10.5281/zenodo.3895860. Lausanne.

[29] GEANT4 geometry from text file version 1.0(n.d.), //geant4.web.cern.ch/sites/default/files/geant4/collaboration/working_groups/geometry/docs/textgeom/textgeom.pdf. (Accessed 1 December 2021).

[30] M.J. Berger, J.S. Coursey, M.A. Zucker, J. Chang, Stopping-power & range tables for electrons, protons, and Helium ions, 2017. //dx.doi.org/10.18434/T4NC7P.

[31] A. Holmes-Siedle, L. Adams, Handbook of Radiation Effects, Second, Oxford University Press, New York, 2002.

[32] R. Baumann, K. Kruckmeyer, Radiation Handbook for Electronics: a compendium of radiation effects topics for space, industrial and terrestrial

applications. www.ti.com/radbook, 2019.
[33] Y. Chen, G. Reeves, R.H.W. Friedel, M.F. Thomsen, M. Looper, D. Evans, J. Sauvaud, LEEM: a new empirical model of radiation-belt electrons in the low-Earth-orbit region, J. Geophys. Res. Sp. Phys. 117 (2012) n/a-n/a. doi.org/10.1029/2012JA017941.
[34] J. Park, K.W. Min, H. Seo, E. Kim, K. Ryu, J. Sohn, J. Seon, J. Yoo, S. Lee, B. Kress, J. Lee, C. Woo, D. Lee, Multi-year statistics of LEO energetic electrons as observed by the Korean NextSat-1, Space Weather 19 (2021), https://doi.org/10.1029/2021SW002787.
[35] C. Zhang, F. Chen, Z. Huang, M. Jia, G. Chen, Y. Ye, Y. Lin, W. Liu, B. Chen, Q. Shen, L. Zhang, E.J. Lavernia, Additive manufacturing of functionally graded materials: a review, Mater. Sci. Eng. 764 (2019), 138209, https://doi.org/10.1016/j.msea.2019.138209.
[36] M.J. Berger, J.H. Hubbell, S.M. Seltzer, J. Chang, J.S. Coursey, R. Sukumar, M.A. Zucker, K. Olsen, XCOM: photon cross section database, 2010. //dx.doi.org/10.18434/T48G6X.